Finite element simulation of hard magnetic properties

T. Schrefl, D. Süss, W. Scholz, J. Fidler

Institute of Applied and Technical Physics, Vienna University of Technology, Wiedner Hauptstraße 8-10, A-1040 Vienna, Austria

Abstract—**Finite element modeling treats magnetization processes within the framework of micromagnetic theory, taking into account the complex microstructure of a magnet. The numerical integration of the Gilbert equation of motion provides the time evolution of the magnetization and thus shows how reversed domain nucleate and expand. The numerical results of static micromagnetic calculations reveal the influence of the intrinsic magnetic properties on the remanence and the coercive field of three different types of permanent magnets: (1) In nucleation controlled Nd-Fe-B magnets, the magnetic properties of intergranular regions control the coercive field. The coercive field decreases with increasing alignment if the grain boundary region with reduced magnetocrystalline anisotropy exceeds 10 nm. (2) In isotropically oriented grains of nanocrystalline magnets, exchange interactions between neighboring soft and hard grains lead to remanence enhancement. An increase of the hard phase anisotropy of only 8% increases the coercive field of two phase $Nd_2Fe_{14}B/\alpha$-Fe magnets significantly. In two phase $Nd_2Fe_{14}B/Fe_3B$, the reduction of the soft phase magnetization and/or the soft phase exchange constant leads to an improvement of the coercive field without a significant loss in remanence. (3) For pinning controlled Sm-Co magnets for high temperature applications a the finite element model was built according to the cellular microstructure. The simulation reveals the upper limits for the coercive field.**

Index Terms—**Finite element method, Permanent magnets, Numerical micromagnetics, Nd-Fe-B, Sm-Co magnets**

I. INTRODUCTION

The micromagnetic theory is an approach to explain the magnetization reversal or hysteresis effects of ferro- and ferri-magnetic materials at an intermediate scale between magnetic domains and crystal lattice sites. Originally in micromagnetics [1] a continuous magnetization vector is used rather than individual atomic moments to describe the details of the transition regions between magnetic domains [2]. Micromagnetism is a generic term used for a wide variety of studies of magnetization structures and reversal mechanisms in magnetic materials. Since the mid 1980´s the improved availability of large scale computer power has enabled the study of increasingly detailed and subtle physical behavior, which has also impacted on the rapid technological development of advanced magnetic materials. The increasing impact of magnetic materials on many modern industries will continue well into the next century. Besides recording materials and soft magnetic devices, also hard magnetic materials are key components in information and transportation technologies, machines, sensors and many other systems.

The finite element method effectively treats the irregular microstructure of permanent magnets [3-4]. Thus precise theoretical predictions of the magnetic properties are possible, taking into account microstructural features such as grain size,

particle shape and intergranular phases. This work reviews the basic micromagnetic effects that determine the remanence and the coercive field of permanent magnets. The interplay of the various effects leads to a complex dependence of the hysteresis properties on the microstructure and the intrinsic magnetic properties.

Finite element models of the grain structure are obtained from a nucleation and growth model and subsequent meshing of the polyhedral regions. Numerical micromagnetics at a sub-grain level involves two different length scale which may vary by orders of magnitude. The characteristic magnetic length scale on which the magnetization changes its direction, is given by the exchange length in soft magnetic materials and the domain wall width in hard magnetic materials. For a wide range of magnetic materials, this characteristic length sale is in the order of 5 nm which should be significantly smaller than the grain size of permanent magnets.

Section II of the paper describes the micromagnetic finite element model. Section III presents numerical calculations of nucleation field of high energy density $Nd_2Fe_{14}B$ magnets. Section IV discusses the influence of the microstructure and the intrinsic magnetic properties an remanence and coercivity of nanocrystalline $(Nd_2Fe_{14}B)_x(Fe_3B/\alpha$-Fe$)_{1-x}$ hard magnets. Section V treats the domain wall pinning in high temperature $Sm(Co,Fe,Cu,Zr)_{7-8}$ magnets. Section VI summarizes the numerical predictions.

II. FINITE ELEMENT MODELS

The hysteresis properties either follow from the direct minimization of the total magnetic Gibb's free energy or from the time integration of the Gilbert equation of motion. The total Gibb's free energy is the sum of the exchange energy, the
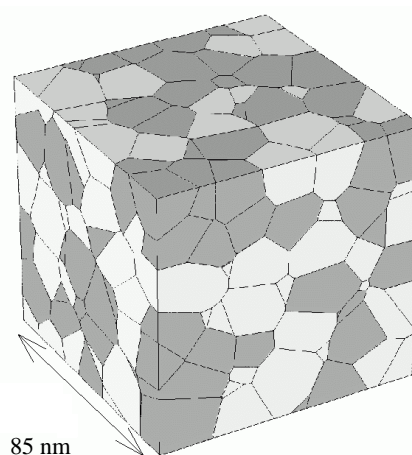

Fig. 1. Finite element model of the grain structure of a two-phase $Nd_2Fe_{14}B/Fe_3B$ magnet a 50 vol% $Nd_2Fe_{14}B$ / 50 vol% Fe_3B magnet, consisting of 343 grains.

magneto-crystalline anisotropy energy, the magnetostatic energy, and the Zeeman energy:

$$E_t = \int \left[A \sum_{i=1}^{3} (\nabla \beta_i)^2 + f_k(\boldsymbol{J}) - \frac{1}{2}\boldsymbol{J} \cdot \boldsymbol{H}_d - \boldsymbol{J} \cdot \boldsymbol{H}_{ext} \right] dV, \quad (1)$$

where $\boldsymbol{J} = (\beta_1, \beta_2, \beta_3) J_s$ denotes the magnetic polarization. A is the exchange constant and f_k is the energy density associated with uniaxial ($Nd_2Fe_{14}B$), cubic (α-Fe), or in-plane (Fe_3B) magnetocrystalline anisotropy. $\boldsymbol{H}_d$ and $\boldsymbol{H}_{ext}$ denote the demagnetizing and the external field, respectively. The minimization of (1) with respect to $\boldsymbol{J}$, subject to the constraint $|\boldsymbol{J}| = J_s$, provides an equilibrium state of the ferromagnetic structure. The numerical minimization method determines the path the system proceeds towards the local minimum. The Gilbert equation

$$\frac{\partial \boldsymbol{J}}{\partial t} = -|\gamma| \boldsymbol{J} \times \boldsymbol{H}_{eff} + \frac{\alpha}{J_s} \boldsymbol{J} \times \frac{\partial \boldsymbol{J}}{\partial t} \quad (2)$$

is believed to give the physical path of the system towards equilibrium. The effective field, $\boldsymbol{H}_{eff} = -\delta E_t / \delta \boldsymbol{J}$, is the variational derivative of the magnetic Gibb's free energy. A Gilbert damping constant $\alpha = 1$ was used.

Realistic models of the grain structure are obtained from a Voronoi construction [5], where the grains are assumed to grow with constant velocity from randomly located seed points. The grains are given by the Voronoi cells surrounding each point. The Voronoi cell of seed point k contains all points of space which are closer to seed point k than to any other seed point. In order to avoid strongly irregular shaped grains, it is possible to divide the model magnet into cubic cells and to choose one seed point within each cell at random. Different crystallographic orientations and different intrinsic magnetic properties are assigned to each grain. In addition, the grains may be separated by an narrow intergranular phase. Once the polyhedral grain structure is obtained, the grains are further subdivided into tetrahedral finite elements. Fig. 1 shows the microstructure of a two-phase nanocrystalline magnet obtained from a Voronoi construction. Alternatively, the microstructure may be directly obtained from TEM images. This method was applied to simulate the nucleation of reversed domains near grain boundary junctions and to calculated the pinning field in precipitation hardened $Sm(Co,Cu,Fe,Zr)_{7-8}$ magnets

Equations (1) or (2) are solved using standard finite element techniques. The numerical details are given in [3-4,6-8].

III. HIGH ENERGY DENSITY $Nd_2Fe_{14}B$ PERMANENT MAGNETS

High energy density magnets exhibit a complex microstructure which is strongly influenced by the processing process. High performance Nd-Fe-B magnets (with an energy density product, $BH_{max} > 400$ kJ/m^3) are produced by the sintering technique, which leads to grain sizes above 1 μm. The doping of elements changes the phase relation and favours the formation of new phases. Additional secondary non-magnetic inter-

granular phases decrease the remanence and interrupt the magnetic interactions between the grains, thereby improving the coercivity of large grained sintered magnets [9]. In magnets with higher Nd-concentrations grain size, misorientation and distribution of grains control the coercive field. The higher the Nd-content of the magnet and therefore the volume fraction of the Nd-rich intergranular phase is, the more reduced is the contribution of the exchange and also dipolar coupling between the grains. Numerical micromagnetic modeling is an effective tool to analyze the influence of intergranular phases on the reversal process.

The micromagnetic model is based on TEM investigations of Nd-Fe-B magnets. The TEM micrograph of Fig. 2 shows the grain junction of three grains and a small amount of Nd-rich phase (the triangular area in the middle of the picture). The upper images of Fig. 1 show the corresponding model of the microstructure which is used for the simulations. The four grains are drawn separately for a better presentation. The dark regions of the upper left picture shows the dispersion of Nd-rich phases. The anisotropy constant is varied in the regions which are drawn dark in the upper right picture of Fig. 2. The arrows in the middle right picture of Fig. 2 represent the projection of the easy axis onto the image plane. For the calculations the material parameters of the $Nd_2Fe_{14}B$ phase at $T = 300$ K has been taken from Sagawa et al. [10] ($K_1 = 4.5 \cdot 10^6$ J/m^3, $J_s = 1.61$ T, $A = 12.5 \cdot 10^{-12}$ J/m).
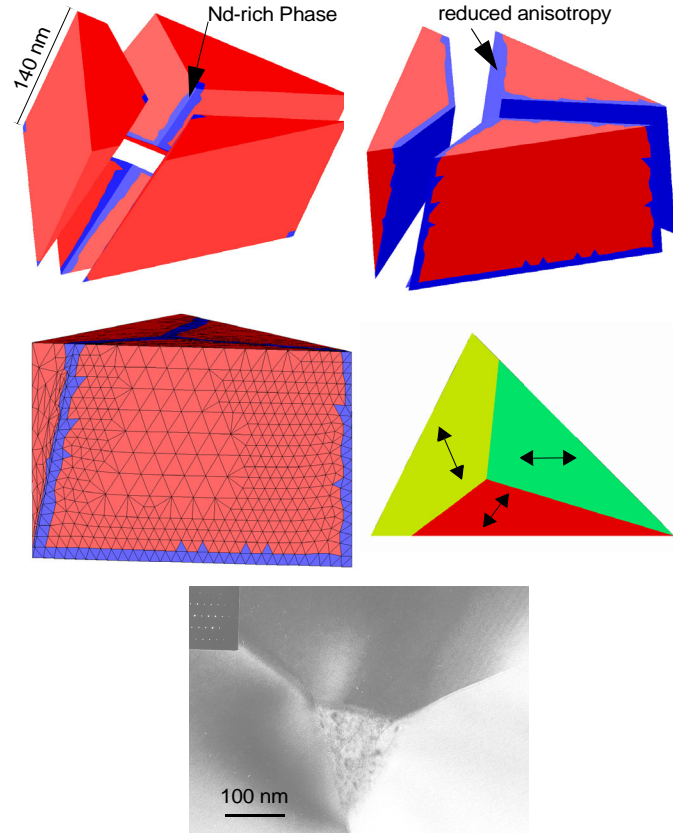

Fig. 2. The upper images show the microstructure for the finite element model. In the dark regions the intrinsic properties are varied. The picture at the bottom shows a TEM micrograph of a Nd-Fe-B sintered magnet.
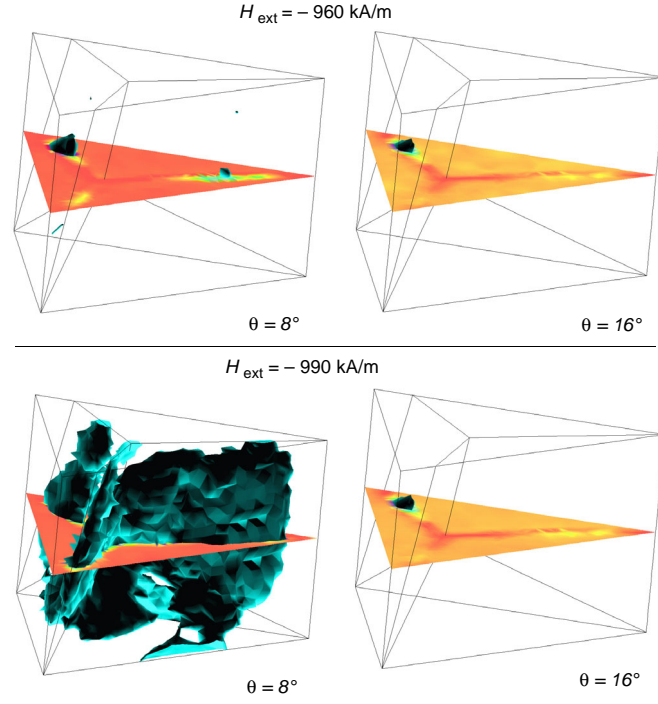
Fig. 3. Nucleation of reversed domains near grain boundaries in high energy density $Nd_2Fe_{14}B$ magnets. The isosurfaces show the regions, where reversed domains are nucleated at H_{ext}=-960 kA/m assuming $K_1 = 0$ in the intergranular region. A perfect alignment leads to a rapid growth of the reversed nucleus. θ denotes the angle between the alignment direction and the easy axis.

A. Perfect grain boundaries

For a perfect microstructure the numerical results agree well with the Stoner-Wohlfarth theory [11]. The most misoriented grain, which has the largest angle between the c-axes and the alignment direction, determines the coercive field. The coercive field decreases with increasing misalignment.

B. Distorted grain boundaries

A reduction of the magneto-crystalline anisotropy near the grain boundaries leads to a linear decrease of the coercive field. The coercive field decreases from 3200 kA/m to 900 kA/m as the anisotropy constant in a 10 nm thick region near the grain boundaries is reduced from its bulk value to zero. The reduction in the magneto-crystalline anisotropy reverses the dependence of the coercive field on the degree of alignment. The coercive field increases by about 80 kA/m as the misalignment angle is changed from 8° to 16°. This effect has to be attributed to a higher demagnetizing field in the well aligned sample which initiates the nucleation of reversed domains within the defect region. The simulations allow to identify the regions within the microstructure where reversed domains are nucleated. Fig. 3 compares the nucleation process for two different degrees of alignment The isosurfaces show the growth of the reversed domains as a function of the applied field.
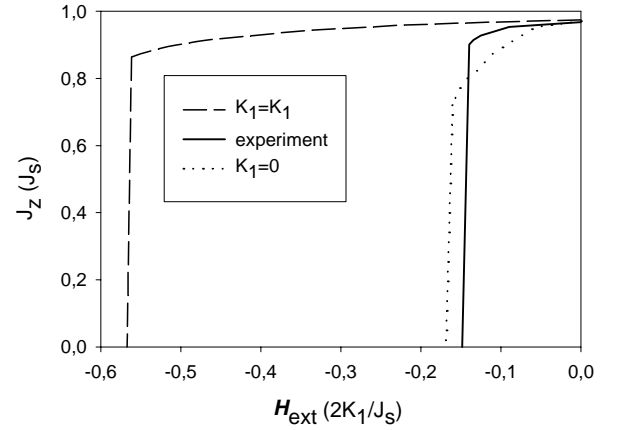

Fig. 4. Comparison of the demagnetizing curves of magnets with perfect grain boundaries and distorted grain boundaries with experimental data

C. Nd-rich boundary phases

The finite element simulations confirm that non-magnetic Nd-rich phases at grain boundary junctions significantly increase the coercive field. For the simulations a Nd-rich phase at the grain boundary junction of three grains is assumed as shown in the upper left picture of Fig. 2. The comparison of the demagnetizing curves of Fig. 4 shows that the coercive field increases by about 15% as non magnetic Nd-rich phases near grain boundary junctions are taken into account. The presence of the Nd-rich phase significantly changes the exchange and the magnetostatic interactions. As a consequence the nucleation of reversed domains is suppressed.

IV. NANOCOMPOSITE PERMANENT MAGNETS

Nanocomposite permanent magnets have been widely studied experimentally and theoretically during the last decade [122-21]. These magnets consists of a mixture of magnetically hard and soft phases. Nanocomposite magnets show a high remanence and a reasonable large coercive field, if both phases are sufficiently exchange coupled. Nanocomposite magnets with excellent hard magnetic properties were obtained for various different compositions. The soft magnetic phase is either α-Fe or Fe_3B. As the hard magnetic phase, $Nd_2Fe_{14}B$, $SmCo_5$, $Sm_2Fe_{14}N_x$, and $Pr_2Fe_{14}B$ were used. Possible application for nanocomposite permanent magnets are bonded magnets used in consumer electronic applications, where the miniaturization requires magnets that are easy to magnetize [22-23]. In addition, the reduction of the total rare-earth content may lead to a cost reduction.

In conventional nanocomposite magnets the hard magnetic grains are randomly oriented. Single phase, isotropic magnets show a remanence J_r of

$$J_r = J_s / 2 \tag{3}$$

if magnetic interactions between the grains are neglected. J_s denotes the saturation polarization. The upper limit for the coercive field of non-interacting particles,

$$H_c = 0.48 \times 2 \, K_1 / J_s, \qquad (4)$$

was given by Stoner and Wohlfarth [11]. K_1 is the magneto-crystalline anisotropy constant. In single phase, nanocrystal-line magnets intergrain exchange interactions enhance the remanence with respect to (3) and reduce the coercive field with respect to (4) [24]. Hadjipanayis and Gong [25] qualitatively explained the relation between remanence and coercivity, applying a molecular-field approach. Fukunaga and Inoue [26] numerically predicted remanence enhancement and the reduction of the coercive field in nanocrystalline permanent magnets, using a three-dimensional finite difference method. In addition to the grain size, the shape of the grains significantly influences the remanence and the coercive field. Two-dimensional finite element calculations [6] show that irregular shaped grains deteriorate the coercive field of isotropic permanent magnets.

D. Remanence Enhancement and Magnetization Reversal

Generally, isotropic permanent magnets with a remanence ration $J_r/J_s > 0.5$ are referred as remanence enhanced materials. However, the theoretical limit for the remanence of noninteracting grains depends on the crystal symmetry, the crystallographic orientation of the easy directions, and the volume fraction and the saturation polarization of the phases [13,27]. The remanence ratio of a two-phase nanocomposite magnet is

$$J_r/J_s = (1/J_s)\{v_1 m_1 J_{s1} + (1 - v_1)m_2 J_{s2}\}, \qquad (5)$$

where m_1 and m_2 denote the remanence ratio of phase 1 and phase 2. Without any interactions, the remanence ratio of $Nd_2Fe_{14}B$ (uniaxial) and Fe_3B (easy-plane) is $m_1 = 0.5$ and $m_2 = 0.79$, respectively.
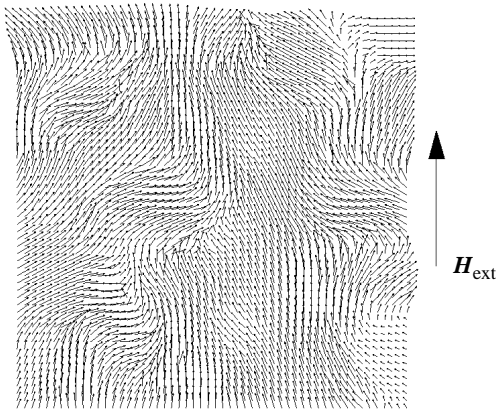

Fig. 5. Remanence enhancement in a two-phase $Nd_2Fe_{14}B/Fe_3B$ magnet containing 343 grains. Top: Finite element model of the grain structure. Bottom: Magnetization distribution in a slice plane for zero applied field. The arrows denote the magnetization direction projected on a slice plane.
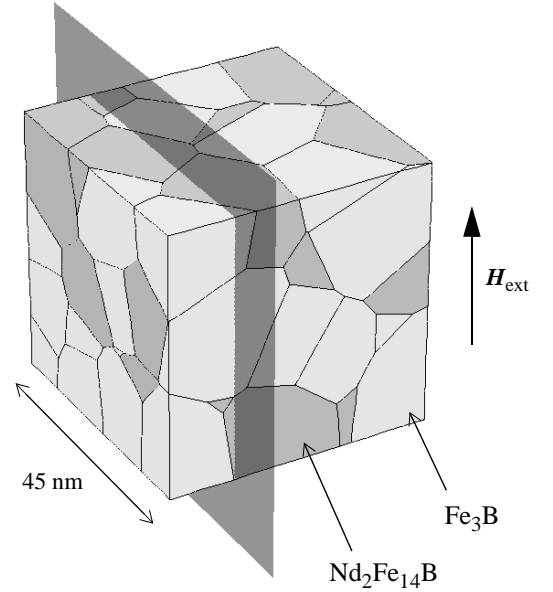

Fig. 6. Model of a nanocomposite magnet used to investigated magnetization reversal dynamics. The volume fraction of the phases is 50% and the mean grain size is 15 nm. The shaded area gives the slice plane used as probe for plots of the magnetization direction.

Fig. 5 gives the calculated magnetization distribution of a 50 vol% $Nd_2Fe_{14}B$ / 50 vol% Fe_3B magnet with a mean grain size of 15 nm for zero applied field. The magnetic polarization J is nearly parallel to the anisotropy direction within the hard magnetic grains. Intergrain exchange interactions determine the direction of J within the Fe_3B grains, where J is parallel to the average magnetization direction of all neighboring $Nd_2Fe_{14}B$ grains. This average direction corresponds to the saturation direction for an isotropic distribution of the hard phase easy axes. The calculated remanence ratio $J_r/J_s = 0.71$ exceeds the theoretical limit for noninteracting particles ($J_r/J_s = 0.65$), given by (5). This result clearly indicates that intergrain exchange interactions enhance the remanence of nanocomposite magnets, provided that the grain size is sufficiently small.

The Gilbert equation of motion (2) was solved for the two-phase $Nd_2Fe_{14}B/Fe_3B$ magnet depicted in Fig. 6. The demagnetization curve, given in Fig. 7 was calculated quasistatically. As an initial condition, the magnetization was set parallel to the saturation field. Then (2) was solved for a positive field of 1120 kA/m until equilibrium was reached. If the change of the magnetic polarization per unit time was smaller than a certain threshold, the external field was decreased by 55 kA/m.

In addition to the equilibrium configurations, the time integration of (2) also reveals the transient magnetic states during irreversible switching. Fig. 7 shows the magnetization distribution for zero applied field and the transient states for $H_{ext} = -450$ kA/m. The time was set to zero, when the external field was switched to $H_{ext} = -450$ kA/m.

Magnetization reversal is dominated by the rotation of the magnetic moments within the Fe_3B grains. During this process, the magnetic polarization of the soft phase remains correlated within an area covering several Fe_3B grains. This
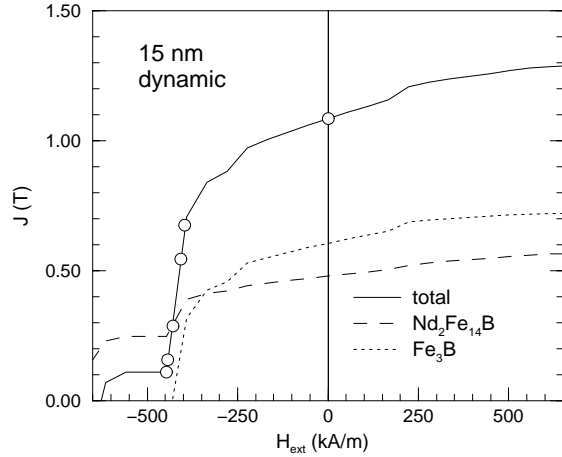
Fig. 7. Quasistatically computed demagnetization curve of a two phase 50 vol% $Nd_2Fe_{14}B$ / 50 vol% Fe_3B magnet. The solid line denotes the total magnetic polarization which is the sum of the contribution of $Nd_2Fe_{14}B$ (dashed line) and of F_3B (dotted line). The circles refer to the magnetization distributions given in fig. 7.
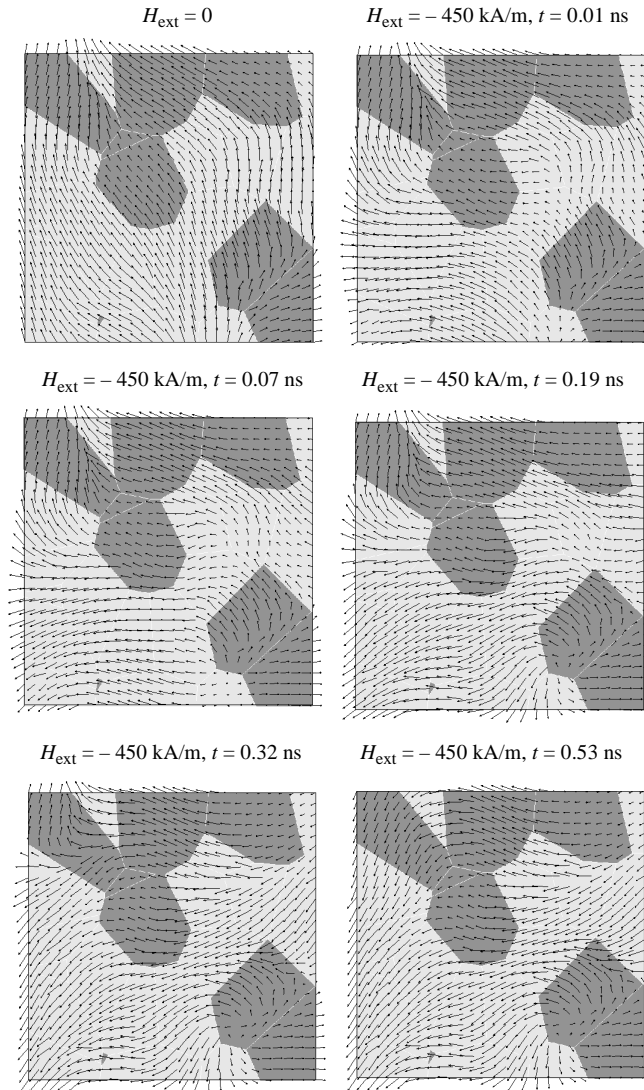

Fig. 7. Remanent state (top left) and transient states at different times t during irreversible switching. The arrows indicate the direction of the magnetic polarization projected on a slice plane.

collective behavior of neighboring soft magnetic grains has to be attributed to exchange interactions. The magneto-crystalline anisotropy hinders the rotation of J within the hard phase, leading to a high exchange energy density at the interface between the different phases. When the expense of exchange energy becomes too high, a reversed domain nucleates within $Nd_2Fe_{14}B$. In what follows, the entire hard magnetic grain becomes reversed. In Fig. 8 this reversal process involves the top left $Nd_2Fe_{14}B$ grain.

E. Influence of Intrinsic Magnetic Properties

The hard magnetic properties of nanocomposite magnets can be significantly improved by modifying the alloy compositions [28]. In micromagnetic calculations it is possible to change the intrinsic magnetic properties accordingly. Table I gives the intrinsic magnetic properties used for the calculations. Literature values for the exchange constant A are only available for $Nd_2Fe_{14}B$ and α-Fe, the values for the other phases are estimated.

TABLE I
INTRINSIC MAGNETIC PROPERTIES

	anisotropy	K_1	K_2	J_s	A
$Nd_2Fe_{14}B$	uniaxial	4.5	0.66	1.61	12.5 [10]
$Nd_2Fe_{14}B$* (increased K_1, K_2; reduced J_s)	uniaxial	4.85	0.72	1.38	12.5
α-Fe	cubic	0.046	0.015	2.15	25 [13]
$Fe_{23}B_6$	cubic	0.01		1.7	17
Fe_3B	easy plane	-0.32		1.62	12.5 [29]
Fe_3B (reduced J_s)	easy plane	-0.32		1.3	12.5
Fe_3B (reduced A)	easy plane	-0.32		1.62	8
Fe_3B (reduced A and J_s)	easy plane	-0.32		1.3	8

Intrinsic magnetic properties: K_1 and K_2 (MJ/m^3), the anisotropy constants; J_s(T), the spontaneous magnetic polarization and the exchange constant A (pJ/m).

The substitution of Nd by Tb or Dy modifies the hard phase properties. An increase of the hard phase anisotropy by 8% and a corresponding reduction of J_s by 14% enhances the coercive field without a significant loss in remanence. Fig. 9 compares the effect of hard phase anisotropy as a function of the Fe_3B content. The mean grain size was 20 nm. Starting from a 40 vol% $Nd_2Fe_{14}B$ / 60 vol% α-Fe magnet, one half of the α-Fe grains were replaced by Fe_3B, giving a $Nd_2Fe_{14}B/\alpha$-Fe/Fe_3B system. Increasing the Fe_3B content improves the coercive field and reduces the remanence. The $Nd_2Fe_{14}B/$ Fe_3B magnet shows a high coercive field but has a bad loop shape. The increase of the anisotropy of only 8% increases the coercive field from 340 kA/m to 450 kA/m in the two phase $Nd_2Fe_{14}B/\alpha$-Fe magnets. The improvement of H_c decreases with increasing Fe_3B content.

The addition of Cr may reduce the magnetization and the exchange constant within the soft magnetic phase [30]. A smaller magnetization results in a lower demagnetizing field which in turn increases the coercivity from 600 kA/m to
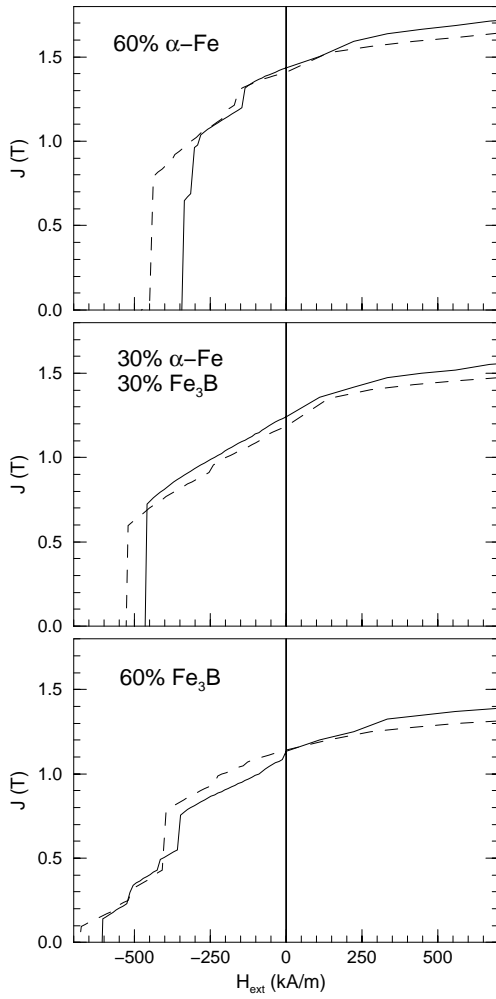
Fig. 8. Effect of enhanced hard phase
anisotropy on the demagnetization curves as a function of the Fe$_3$B content. Solid line: Hard phase is Nd$_2$Fe$_{14}$B, dashed line: hard phase anisotropy increased by 10% and J_s decreased by 14% with respect to Nd$_2$Fe$_{14}$B.

Fig. 9. Influence of the intrinsic magnetic properties on remanence and coercivity in nanocomposite Nd$_2$Fe$_{14}$B-based magnets

ropy. The magnetic polarization and the exchange constant are higher than in Nd$_2$Fe$_{14}$B or Fe$_3$B. Replacing α-Fe by Fe$_{23}$B$_6$ in a two-phase Nd$_2$Fe$_{14}$B/α-Fe magnet reduces the remanence and increases the coercive field. The magnetic properties of the two-phase Nd$_2$Fe$_{14}$B/Fe$_{23}$B$_6$ magnet are intermediate between those of a Nd$_2$Fe$_{14}$B/α-Fe and Nd$_2$Fe$_{14}$B/Fe$_3$B.

Fig. 10 summarizes the effects of the intrinsic magnetic properties of the different phases on the remanence and the coercive field of nanocomposite magnets containing 40 vol% Nd$_2$Fe$_{14}$B with a mean grain size of 20 nm. The plot gives the magnetic polarization for zero applied field and the coercive field in the (H_c, J_r)-plane for different compositions. The solid line gives the change of the magnetic properties with decreasing α-Fe and increasing Fe$_3$B content. The coercive field increases with increasing Fe$_3$B content at the expense of the remanence.

V. PRECIPITATION HARDENED, HIGH TEMPERATURE SM(CO,CU,FE,ZR)$_{7-8}$ MAGNETS

The search for novel soft and hard magnetic materials for high temperature advanced power applications is worldwide an active area of research. The increase of the operating temperature of motors, generators and other electronic devices leads to an improvement of their efficiency. In the development of high temperature magnets the activities concentrate on the improvement of precipitation hardened Sm(Co,Fe,Cu,Zr)$_{7-8}$ magnets and on the search for new compounds with sufficient high values of magnetization and coercive field at elevated

800 kA/m keeping a remanence of about 1.1 T. A reduction of the exchange constant within Fe$_3$B deteriorates the loop shape but increases the coercive field. A reduced exchange constant within the soft magnetic phase decreases the exchange energy density stored at the interface between the soft and the hard magnetic phase. The magnetic polarization within the soft phase may reverse without the immediate nucleation of a reversed domain in neighboring hard magnetic grains. The coupling between the different phases remains large enough to obtain a reasonable loop shape.

Nd$_2$Fe$_{14}$B based nanocomposite magnets may contain a large volume fraction of Fe$_{23}$B$_6$ [13]. This metastable soft magnetic phase has a weak cubic magneto-crystalline anisot-
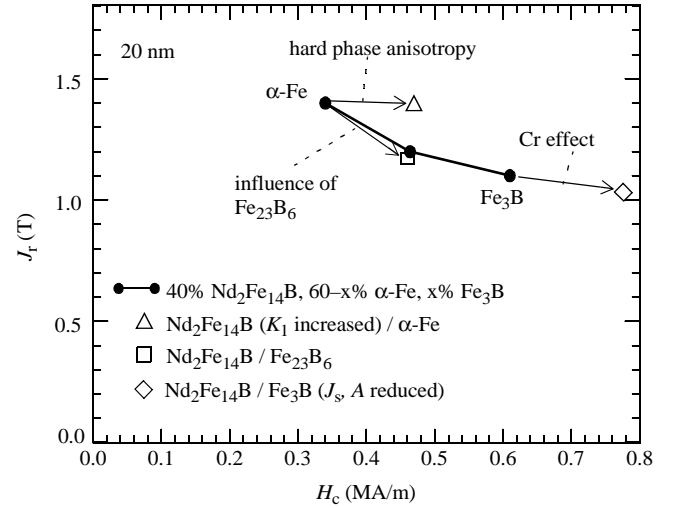
temperatures. A new series of magnets with $_JH_c$ up to 1050 kA/m at 400°C has been developed [31-32]. These magnets have low temperature coefficients of $_JH_c$ and a straight line B vs. H (extrinsic) demagnetization curve up to 550°C. High Cu-, low Fe- and a higher Sm-concentration were found to contribute to high coercivity at high temperatures. TEM investigations show a cellular precipitation structure with about 60 x 120 nm in size [33]. The rhombic cells of the type $Sm_2(Co,Fe)_{17}$ are separated by a $Sm(Co,Cu,Zr)_{5-7}$-cell boundary phase. The development of the continuous, cellular precipitation structure is controlled by the growth process and the chemical redistribution process and is determined by the direction of zero deformation strains due to the lattice misfit between the different phases.

Fig. 11 presents the finite element model of the cellular microstructure, consisting of 27 cells. The model was built according to the cellular microstructure obtained from TEM investigations. The cells are divided into tetrahedral finite elements. The total number of finite elements ranges from about 100.000 to 200.000, depending on the cell size. In order to account for the magnetization transition near the domain walls, we use a so-called geometrical mesh [34]. The mesh is gradually refined towards the cell boundary phase, reaching a mesh size comparable to the domain wall width near the cell boundaries. Table II summarizes the intrinsic magnetic properties used for the calculations. The first two sets of parameter were taken from [35]. The magneto-crystalline anisotropy of the cell boundary phase is reduced as compared the anisotropy of the matrix phase. As a consequence the wall energy is lower within the cell boundary which gives rise to attractive domain wall pinning. Durst and co-workers [35] derived the intrinsic magnetic properties of the cell matrix $Sm_2(Co,Fe)_{17}$ and the cell boundary $Sm(Co,Cu,Zr)_{5-7}$ from the analysis of magnetization curves parallel and perpendicular to the alignment direction. The anisotropy constant of the cell matrix is about 2.6 times larger than the anisotropy constant of the cell boundary phase. The exchange constant was assumed to be the same for both phases, because of similar values of the Curie temperature. The exchange constant was derived from the effective
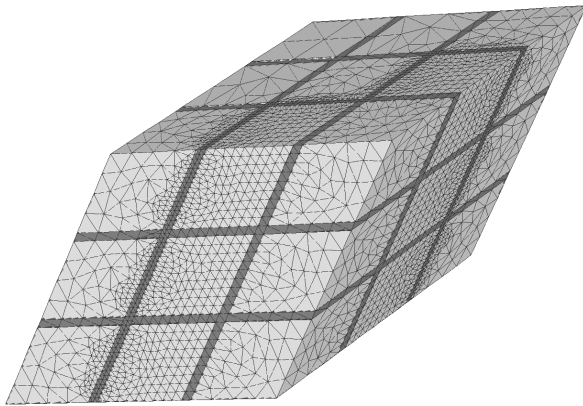
TABLE II
INTRINSIC MAGNETIC PROPERTIES

	T	J_s (T)	K_1 (MJ/m³)	A (pJ/m)	δ_0 (nm)
$Sm_2(Co,Fe)_{17}$ /matrix	300 K	1.3	5	14	1.67
$Sm(Co,Cu,Zr)_{5-7}$ / boundary	300 K	0.8	1.9	14	2.71
$Sm_2(Co,Fe)_{17}$ /matrix	400 K	1.23	3.3	12.6	1.95
$Sm(Co,Cu,Zr)_{5-7}$ / boundary	400 K	0.76	1.1	12.6	3.38
$Sm_2(Co,Fe)_{17}$ / matrix	-	1.3	5	14	1.67
$Sm(Co,Cu,Zr)_{5-7}$ / boundary	-	0.8	7.76	14	1.34

Temperature T and intrinsic magnetic properties: K_1 and K_2 (MJ/m³), the anisotropy constants; J_s(T), the spontaneous magnetic polarization and the exchange constant A (pJ/m) and the Bloch parameter $\delta_0 = (A/K_1)^{1/2}$.

wall energy which was obtained from closure domains of a $Sm(Co,Fe,Cu,Zr)_{7.6}$ magnet. The second set of parameters are used to model repulsive pinning. Here the K_1 value of the cell boundary phase is higher than that of the matrix phase. In addition, table II lists the Bloch parameter $\delta_0 = (A/K_1)^{1/2}$, which gives the minimum extension of magnetic inhomogenities.

F. Attractive pinning

The pinning field was calculated as a function of the cell boundary width for the intrinsic magnetic properties at T = 300 K and T = 400 K. The initial state for the calculations is a two-domain state. The subsequent minimization of (1) for increasing external field simulates the motion of the domain wall towards the cell boundary phase. The external field is applied parallel to the c-axis. With increasing field, the domain with the magnetization parallel to the field direction grows. The domain will become pinned at the grain boundary phase.

Fig. 10. Finite element model of the cellular structure of a the $Sm(Co,Fe,Cu,Zr)_{7-8}$ magnet. The bright and dark regions denote the rhombohedral cells and the cell boundary phase, respectively.
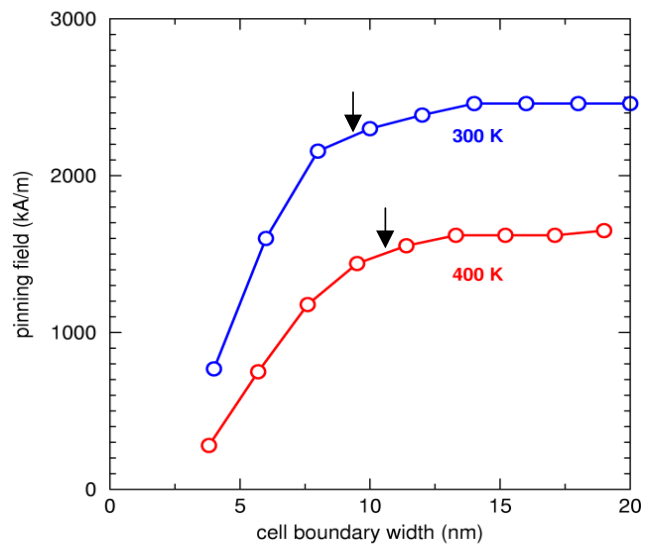

Fig. 11. Calculated pinning field as a function of the cell size for 300 K and 400 K. The arrows indicate the domain wall width $\pi\delta_0$ of the cell boundary phase.
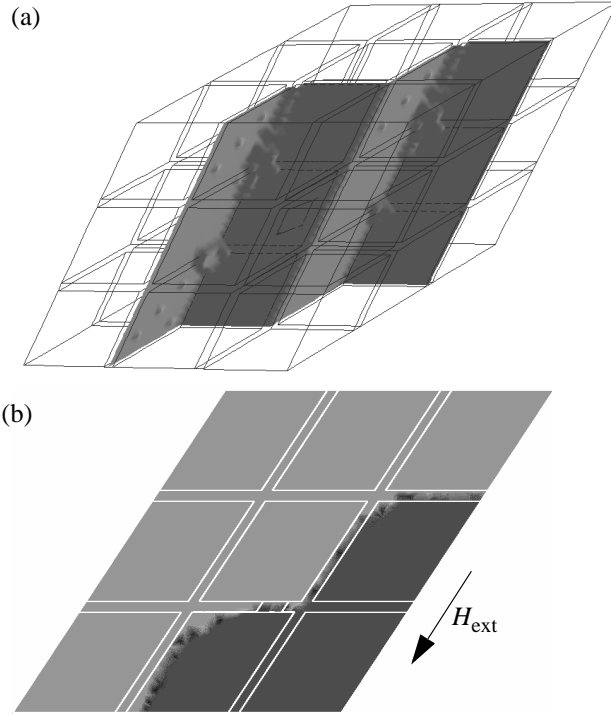
(a)

(b)

H_{ext}

Fig. 12. (a) Interaction of a domain wall with the cellular structure. The 3D images give the trace of the domain wall at H_{ext} = 1.8 MA/m. (b) Depinning of the domain wall at H_{ext} = 2.4 MA/m. The grey scale maps magnetization components parallel to the c-axis.

Fig. 12 gives the pinning field as function of the cell boundary width for 300 K and 400 K. The decrease of the maximum pinning field with increasing temperature has to be attributed to the decrease of $\Delta K_1 = K_1^{matrix} - K_1^{boundary}$ from ΔK_1 = 3.1 MJ/m³ to ΔK_1 = 2.2 MJ/m³. In order to obtain the maximum pinning fields (2.4 MA/m at 300 K and 1.6 MA/m at 400 K), the cell boundary width must exceed the domain wall width, $\pi\delta_0$, of the cell boundary phase. The pinning field at 300 K reaches only 1 MA/m to 2 MA/m for a cell boundaries thickness of 3 nm and 6 nm, respectively. Fig. 13a shows the trace of the domain wall within the cellular microstructure at an applied field of 1.8 MA/m. As the external field is increased the wall breaks away from cell boundary phase. Depinning of the domain wall starts at the corners of the cell boundary. This process is illustrated in fig. 13b which gives a the calculated domain pattern a slice plane parallel to the c-axis for an applied fields of 2.4 MA/m

G. Repulsive Pinning

Finally, the pinning field owing to repulsive pinning was calculated, using the parameter set 3 of table I. The pinning field was in the range from 2.1 MA/m to 2.6 MA/m for a thickness of the cell boundary phase of 6 nm and 10 nm, respectively. The wall is pushed towards the cell boundary phase. As the wall energy is higher within the cell boundary phase, the center of the wall remains in the matrix phase.
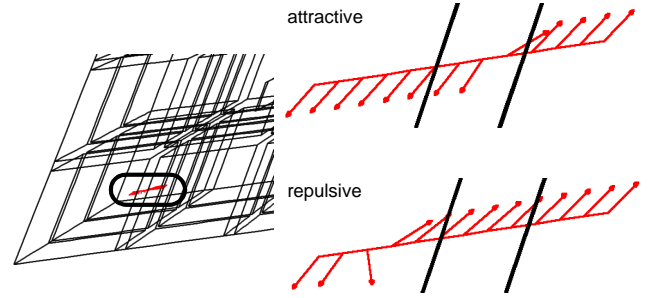

attractive

repulsive

Fig. 13. Computed magnetization configuration for attractive and repulsive pinning.

Fig. 14 compares the computed magnetization structure within the domain wall for attractive and repulsive pinning.

VI. SUMMARY

Finite element micromagnetic simulations compute the local arrangement of the magnetic moments under the influence of the microstructure and the intrinsic magnetic properties. The numerical results provide a better understanding of the influence of the microstructure on the magnetic properties of permanent magnets.

High energy density Nd-Fe-B magnets

Distorted grain boundaries reduce the coercive field of nucleation controlled, high-energy density Nd-Fe-B magnets. In contrast to the Stoner-Wohlfarth theory the coercive field will increase with decreasing alignment of the easy axis if the anisotropy is reduced near grain boundaries. The finite element simulations confirm the experimental results that non-magnetic Nd-rich phases at grain boundary junctions significantly increase the coercive field.

Nanocomposite magnets

The magnetic properties of nanocomposite permanent magnets may be improved tailoring the hard phase anisotropy or the soft phase exchange constant. The substitution of Nd by Tb or Dy increases the hard phase anisotropy and reduces the saturation polarization. The coercivity of two phase $Nd_2Fe_{14}B/\alpha$-Fe magnets can be improved by about 30% without a significant loss in remanence. The addition of Cr reduces the soft phase exchange constants causing to an increase of the coercive field in two-phase $Nd_2Fe_{14}B/Fe_3B$ magnets.

High-temperature magnets

The coercive field in high-temperature $Sm(Co,Fe,Cu,Zr)_{7-8}$ results from domain wall pinning at the cellular precipitation structure. A minimum width of the cell boundary phase is necessary to obtain high pinning fields. With decreasing anisotropy K_1 of the cell boundary phase, the thickness D of the cell boundary phase has to be increased in order to meet the condition $D > \pi\delta_0$.

REFERENCES

[1] W. F. Brown Jr., *Micromagnetics*. New York: Wiley, 1963.

[2] L. Landau and E. Lifshitz, "On the Theory of Magnetic Permeability in Ferromagnetic Bodies.," Physik. Z. Sowjetunion, vol. 8, pp. 153, 1935.

[3] T. Schrefl, R. Fischer, J. Fidler, and H. Kronmüller, "Two- and Three-Dimensional Calculation of Remanence Enhancement of Rare-Earth Based Composite Magnets (Invited)," *J. Appl. Phys.*, vol. 76, pp. 7053-7058, 1994.

[4] T. Schrefl and J. Fidler, "Modelling of exchange-spring permanent magnets," *J. Magn. Magn. Mater.*, vol. 177, pp. 970-975, 1998.

[5] F. P. Preparata, *Computational Geometry*: Springer, 1985.

[6] T. Schrefl, J. Fidler, and H. Kronmüller, "Remanence and coercivity in isotropic nanocrystalline permanent magnets," Phys. Rev. B, vol. 49, pp. 6100-6110, 1994.

[7] T. Schrefl, H. Roitner, and J. Fidler, "Dynamic Micromagnetics of Nano-composite NdFeB Magnets," *J. Appl. Phys.*, vol. 81, pp. 5567-5569, 1997.

[8] T. Schrefl, J. Fidler, K. J. Kirk, and J. N. Chapman, "A Higher Order Fem-Bem Method For the Calculation of Domain Processes in Magnetic Nano-Elements," *IEEE Trans. Magn.*, vol. 33, pp. 4182-4184, 1997.

[9] J. Fidler, "Rare earth intermetallic magnets," in *Inst. Phys. Conf. Ser.* No.152, Section G: Magnetic Materials, 1998, pp. 805-813.

[10] M. Sagawa, S. Fujimura, N. Yamamoto, Y. Matsuura, and S. Hirosawa, "Magnetic properties of rare-earth-iron-boron permanent magnet materials," *J. Appl. Phys.*, vol. 57, pp. 4094-4096, 1985.

[11] E. C. Stoner and E. P. Wohlfarth, "A mechanism of magnetic hysteresis in heterogeneous alloys," *Philos. Trans. R. Soc.*, vol. 240, pp. 599-642, 1948.

[12] R. Coehoorn, D. B. De Mooij, and C. De Waard, "Meltspun permanent magnet materials containing Fe_3B as the main phase," *J. Magn. Magn. Mater.*, vol. 80, pp. 101-104, 1989.

[13] E. F. Kneller, "The exchange-spring material: a new material principle for permanent magnets," *IEEE Trans. Magn.*, vol. 27, pp. 3588-3600, 1991.

[14] H. Kanekiyo, M. Uehara, and S. Hirosawa, "Microstructure and Magnetic Properties of High-Remanence $Nd_5Fe_{14.5}Co_5B_{18.5}M$ (M=Al, Si, Ga, Ag, Au) Rapidly Solified and Crystallized Alloys for Resin-Bonded Magnets," *IEEE Trans. Magn.*, vol. 29, pp. 2863-2865, 1993.

[15] R. Skomski and J. M. D. Coey, "Giant energy product in nanostructured two-phase magnets," *Phys. Rev. B*, vol. 48, pp. 15812-15816, 1993.

[16] H. A. Davies, "Nanocrystalline Exchange-Enhanced Hard Magnetic Alloys," *J. Magn. Magn. Mater.*, vol. 158, pp. 11-14, 1996.

[17] J. Kuma, N. Kitajima, Y. Kanai, and H. Fukunaga, "Maximum energy product of isotropic Nd-Fe-B-based nanocomposite magnets," J. Appl. Phys., vol. 83, pp. 6623-6625, 1998.

[18] R. Fischer, T. Leineweber, and H. Kronmüller, "Fundamental Magnetization Processes in Nanoscaled Composite Permanent Magnets," *Phys. Rev. B*, vol. 57, pp. 10723-10732, 1998.

[19] P. G. McCormick, W. F. Miao, P. A. I. Smith, J. Ding, and R. Street, "Mechanically alloyed nanocomposite magnets (invited)," *J. Appl. Phys.*, vol. 83, pp. 6256-6261, 1998.

[20] D. Goll, M. Seeger, and H. Kronmüller, "Magnetic and microstructural properties of nanocrystalline exchange coupled PrFeB permanent magnets," *J. Magn. Magn. Mater.*, vol. 185, pp. 49-61, 1998.

[21] Y. H. Gao, J. H. Zhu, Y. Q. Weng, E. B. Park, and C. J. Yang, "The enhanced exchange coupled interaction in nanocrystalline $Nd_2Fe_{14}B$/$Fe_3B+\alpha$-Fe alloys with improved microstructure," *J. Magn. Magn. Mater.*, vol. 191, pp. 146-152, 1999.

[22] V. Panchanathan, "Studies on low rare earth Nd-Fe-B compositions," *IEEE Trans. Magn.*, vol. 31, pp. 3605-3607, 1995.

[23] J. J. Croat, "Current Status and Future Outlook For Bonded Neodymium Permanent Magnets," *J. Appl. Phys.*, vol. 81, pp. 4804-4809, 1997.

[24] R. W. McCallum, A. M. Kadin, G. B. Clemente, and J. E. Keem, "High performance isotropic permanent magnets based on Nd-Fe-B," *J. Appl. Phys.*, vol. 61, pp. 3577-3579, 1987.

[25] G. C. Hadjipanayis and W. Gong, "Magnetic hysteresis in melt-spun Nd-Fe-Al-B-Si alloys with high remanence," *J. Appl. Phys.*, vol. 64, pp. 5559-5561, 1988.

[26] H. Fukunaga and H. Inoue, "Effect of intergrain exchange interaction on magnetic properties in isotropic Nd-Fe-B magnets," *Jpn. J. Appl. Phys.*, vol. 31, 1992.

[27] K. H. Müller, D. Eckert, A. Handstein, M. Wolf, S. Wirth, and L. M. Martinez, "Viscosity and Magnetization Processes in Annealed Melt-Spun $Nd_4Fe_{77}B_{19}$," in *8th Int. Symposium on Magnetic Anisotropy and Coercivity in RE-TM Alloys*, C. A. F. Manwaring, D. G. R. Jones, A. J. Williams, and I. R. Harris, Eds. Birmingham: University of Birmingham, 1994, pp. 179-186.

[28] H. Kanekiyo and S. Hirosawa, "Thick $Fe_3B/Nd_2Fe_{14}B$ nanocomposite permanent magnet flakes prepared by slow quenching," *J. Appl. Phys.*, vol. 83, pp. 6265-6267, 1998.

[29] W. Coene, F. Hakkens, R. Coehoorn, D. B. de Mooij, C. de Waard, J. Fidler, and R. Grössinger, "Magnetocrystalline anisotropy of Fe_3B, Fe_2B, and $Fe_{1.4}Co_{0.6}B$ as studied by Lorentz electron microscopy, singular point detection and magnetization measurements," *J. Magn. Magn. Mater.*, vol. 96, pp. 189-196, 1991.

[30] P. A. I. Smith, J. F. O'Sullivan, and J. M. D. Coey, "Structure and magnetic properties of Nd-Tb-Fe-Cr-B nanocomposites produced via mechanical milling," in *15th Int. Workshop on RE Magnets and Their Application*, vol. 1, L. Schultz and K.-H. Müller, Eds. Dresden: Werkstoff-Informationsgesellschaft, 1998, pp. 205-214.

[31] S. Liu, J. Yang., G. Doyle, G. E. Kuhl, C. Chen, and M. Walmer, "New sintered high temperature Sm-Co based permanent magnet materials, " *IEEE Trans. Magn.*, vol. 35, pp. 3325-3327, 1999.

[32] W. Tang, Y. Zhang, and G. C. Hadjipanayis, "Effect of Zr on the microstructure and magnetic properties of Sm(Co,Fe,Cu,Zr)8.5 magnets," J. Appl. Phys., vol. 87, pp. 399-403, 2000.

[33] J. Fidler, P. Skalicky, and F. Rothwarf, "High resolution electron microscope study of $Sm(Co,Fe,Cu,Zr)_{7.5}$ magnets," *IEEE Trans. Magn.*, vol. 19, pp. 2041-2043, 1983.

[34] B. Szabo and I. Babuska, *Finite element analysis*. New York: John Wiley & Sons, 1991.

[35] K.-D. Durst, H. Kronmüller, and W. Ervens, "Investigations of the magnetic properties and demagnetization processes of an extremely high coercive Sm(Co,Cu,Fe,Zr)7.6 permanent magnet I. Determination of Intrinsic Magnetic Properties," *phys. stat. sol. (a)*, vol. 108, pp. 403-416, 1988.